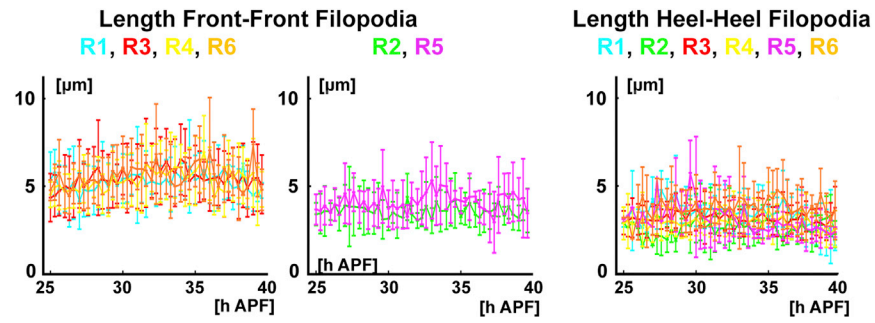


**Figure S1. The Scaffold Remains Stable throughout the Sorting Process, Related to Figure 3**

Fixed preparations of co-labelings of GH146-Gal4 driven CD4-tdGFP in L-cells (green) and anti-Chaoptin labeling of R-cells (red) from 20h APF (first row) through 40h APF (last row). At 20h-35h APF individual heel positions can be determined by following the axons (column 3D traced). In the co-labeling of the lamina plexus, the heel positions are visible as black regions encircled by Chaoptin labeling. The heel scaffold and distances between cartridge centers remain stable between 20h-35h APF (comp. Figure 3K). Scale bars, 5  $\mu$ m.



**Figure S2. Front and Heel Filopodia Extend Characteristic Distances, Related to Figure 4**

(Left panel) The longest front filopodia of R1, R3, R4 and R6 explore furthest between 30-35h, on average one cartridge diameter  $D$  ( $\sim 5.5 \mu\text{m}$ ). (Middle panel) The longest front filopodia of R2 and R5 explore less than  $4 \mu\text{m}$  distance throughout the entire sorting period. (Right panel) The longest heel filopodia reveal shorter extensions than front filopodia. Data shown are mean  $\pm$  SD.

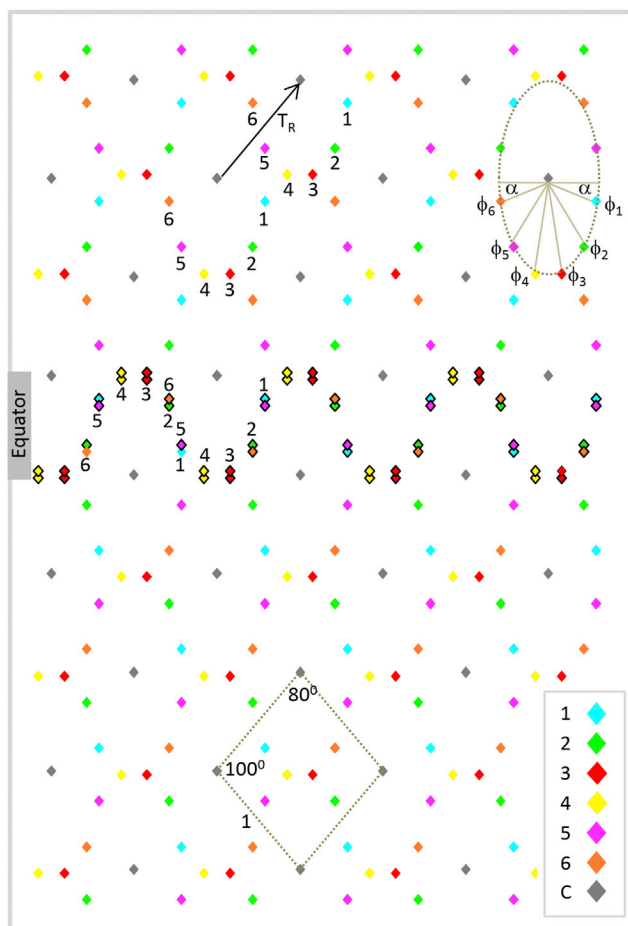
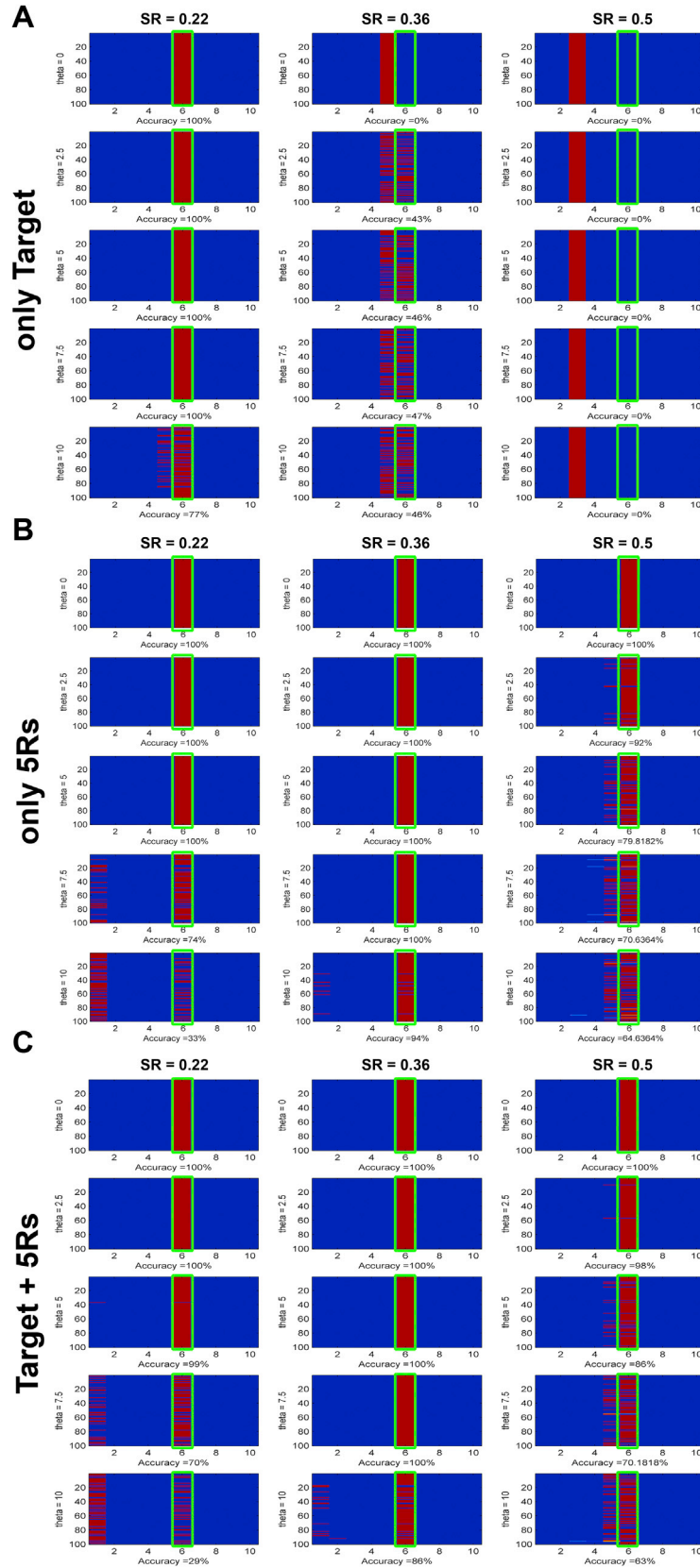


**Figure S3. Quantitative Features of the Scaffold, Related to Figure 5**

Based on measurements in the imaging data, the scaffold is a rhomboidal grid ( $80^\circ/100^\circ$  grid). The grid is uninterrupted across the equator, but the density of R-cells is locally increased with doubly occupied slots. The scaffold is computationally set up based on the cartridge distance  $T_R$  and the angles as described in detail in the [Supplemental Experimental Procedures](#).



(legend on next page)

---

**Figure S4. Simulations of Wiring Accuracy with Random Angle Variation, Related to Figure 6**

(A–C) Shown are simulations for a sensing radius  $SR = 0.22$  (left column),  $SR = 0.36$  (middle column) and  $SR = 0.5$  (right column). (A) Simulations for the 'only target' stop rule, (B) 'overlap with 5 other R-cells' stop rule; (C) 'overlap with target plus 5 other R-cells' stop rule. For each stop rule the first row shows 100 independent runs with no random angle variation, the second row 2.5 degree random variation, the third row 5 degree, the fourth row 7.5 degree, and the fifth row 10 degree random angle variation. All subtypes were independently varied randomly for each of the 100 runs shown in each plot. The green box marks the correct results of 6 terminals per cartridge. Orange marks results obtained in each run. Note that the 'only target' model fails with larger sensing radii, whereas the 'combinatorial overlap' stop rules function best with an intermediate sensing radius.

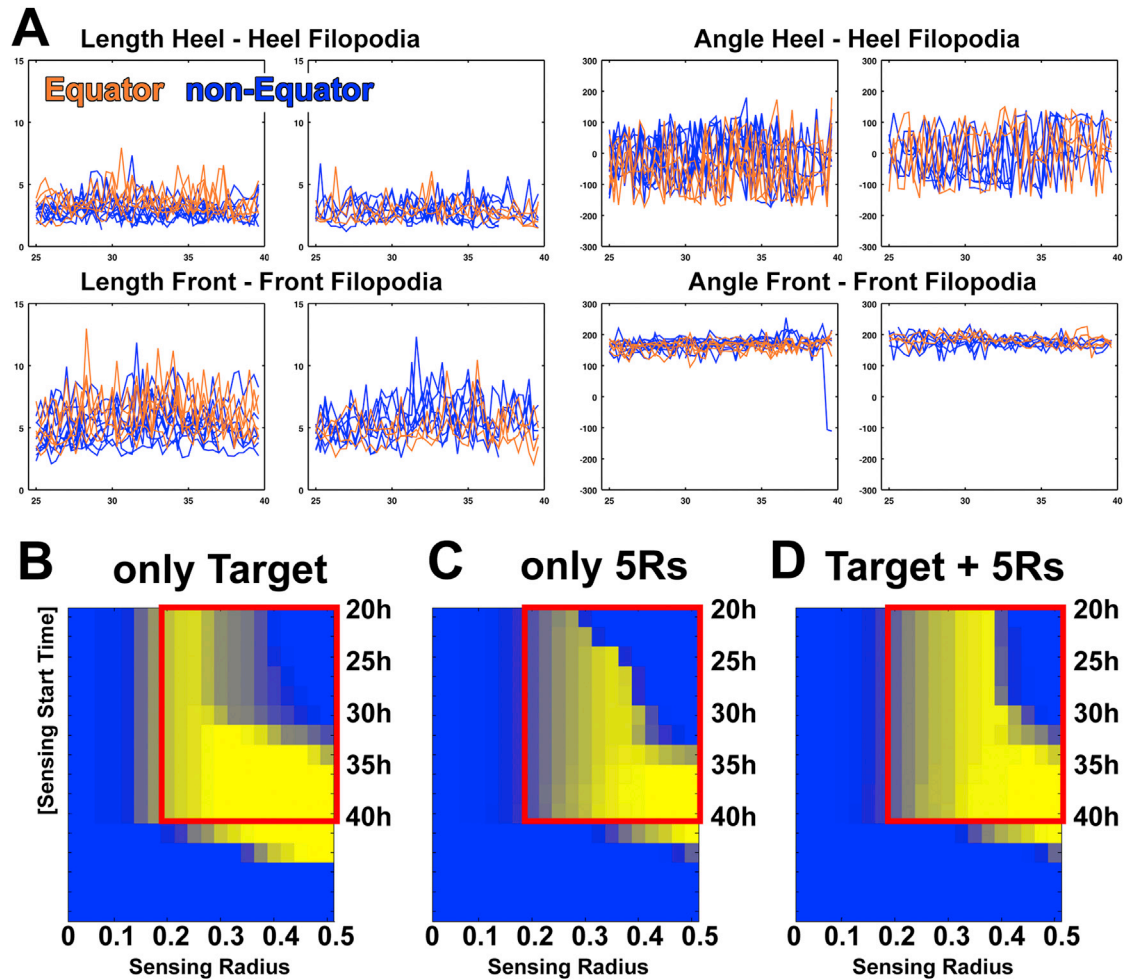
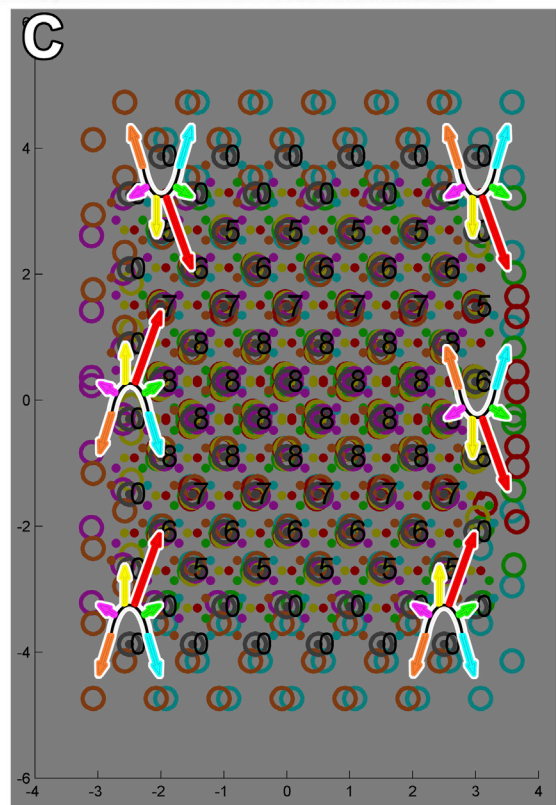
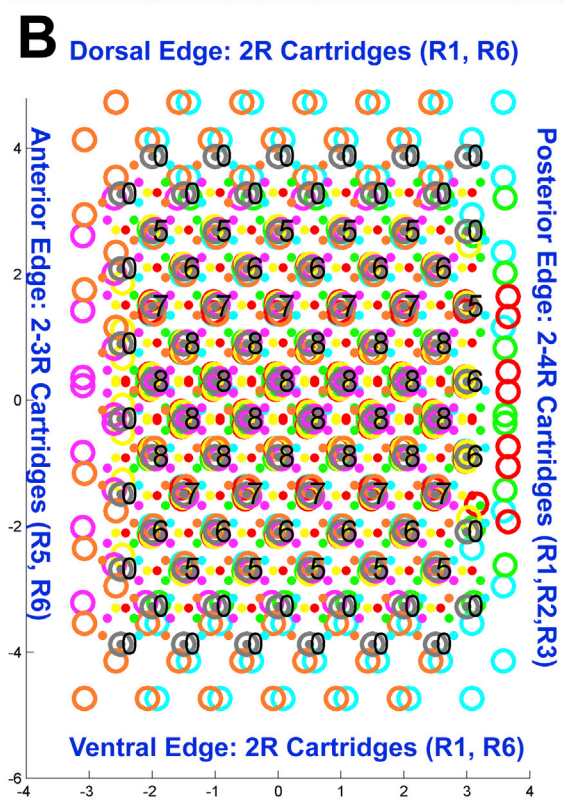
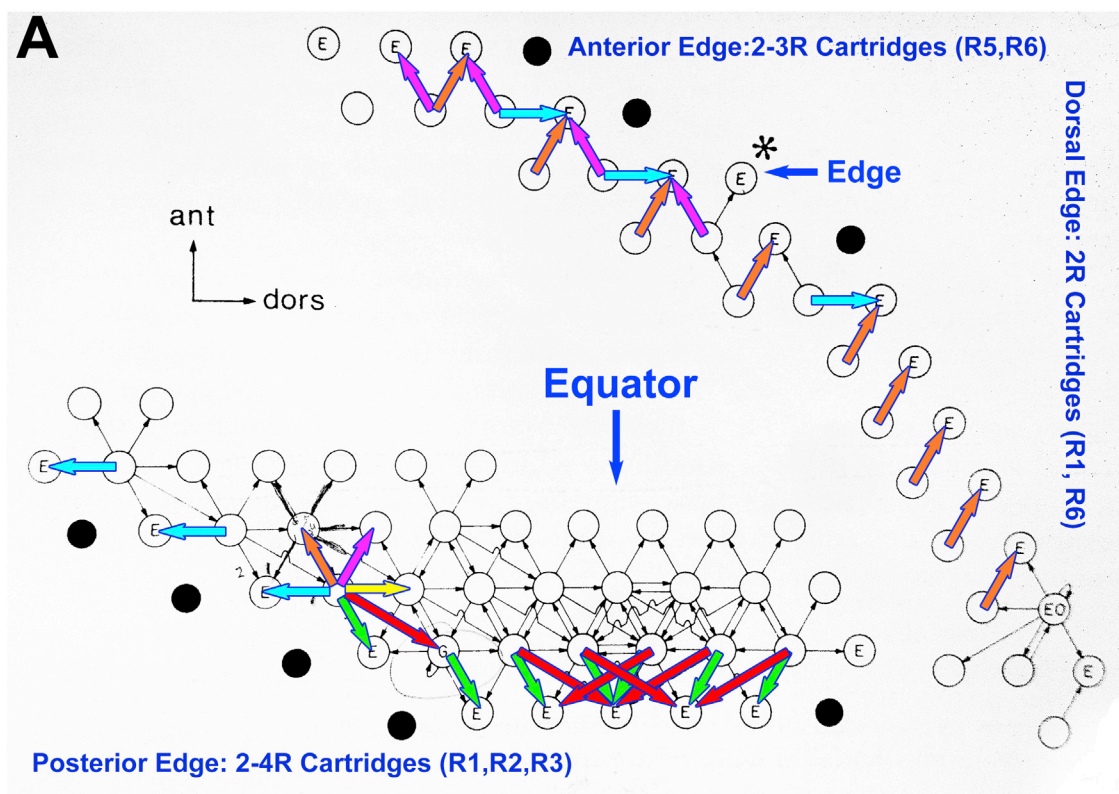


**Figure S5. Wiring Accuracy at the Equator, Related to Figure 7**

(A) Measurements of the lengths and angles of heel-heel and front-front filopodia reveal identical dynamics between equator and non-equator growth cones. (B–D) Systematic scans for sensing radii 0–0.5, sensing start time 20–40h and  $\pm 10^\circ$  randomly varied extension angles similar to Figures 6K–6M, but specifically for the equator region. (B) Simulations for the ‘only target’ rule and two combinatorial stop rules without (C) and with target (D). Each data point was simulated 100 times for angles that were randomly offset  $\pm 10^\circ$ .



(legend on next page)

---

**Figure S6. Analysis of Edge Cartridges, Related to Figure 7**

(A) Edge cartridge analysis adapted from Figure 25 of [Meinertzhagen and Hanson \(1993\)](#). The border of the lamina provides, in addition to the equator, a second region of naturally occurring cartridges that do not contain the precise R1–R6 neural superposition wiring. Edge cartridges have been analyzed in detail as reported by [Meinertzhagen and Hanson \(1993\)](#) for individual *Musca* and *Drosophila* specimens. Edge cartridges lack an overlying ommatidium in the retina. They receive input from R growth cones from the interior of the lamina and hence contain less than six R terminals. However, the development of edge cartridges is less straight forward than equator cartridges for two reasons: first, the nature of the border of the lamina and its influence on growth cone extension and stop is unclear, whereas at the equator the homogeneous target grid is uninterrupted and no special border conditions apply. Second, edge cartridges are originally innervated by an overlying ommatidial axon bundle from ommatidia in the retina's margin that degenerate prior to eclosion (Wolff and Ready, 1991). The involvement of degenerating axons is only obvious in a small time window around 44h APF ([Meinertzhagen and Hanson, 1993](#)). However, occasional marginal R-cells and their innervations survive, causing irregularities in wild-type edge cartridges, as described below. Despite these complications, [Meinertzhagen and Hanson \(1993\)](#) report the following key observations on edge cartridges: First, edge cartridges receive for the most part exactly those R terminal inputs from inside the lamina that neural superposition wiring dictates. Second, similar to the equator region, the edge is a region of decreased wiring robustness, i.e., R growth cone projection errors are observed in wild-type that almost never occur in neural superposition cartridges.

(B and C) Simulation of the 3-rule model predicts the observations made in (A). First, the extension of R1–R6 growth cones with constant angles predicts precisely which R front should 'hit the border' of the lamina on all sides. Second, any stop rule that is based on R front interactions is likely to fail in cartridges where number of interacting R fronts vary; at the equator, a higher density of R fronts causes more likely premature stops, whereas at edge cartridges a reduced number of R fronts may permit incorrect extensions, although the unknown role of the border itself confounds precise predictions. Both observations are apparent in a model simulation that includes the edges. Each edge at and away from the equator receives a specific complement of R fronts. Both the dorsal and ventral edge receive exclusively R1 and R6 fronts, leading to 2R edge cartridges (B, C). In contrast, the anterior edge receives exclusively R5 and R6 fronts and the posterior edge receives R1, R2 and R3 with increased density at the equator compared to the main lamina, leading to 2R, 3R and 4R edge cartridges (B, C). These data largely match the observations by [Meinertzhagen and Hanson \(1993\)](#) shown in (A). However, since the lamina has curved edges not all edge cartridges can be precisely predicted. In addition, the simulation reveals how an R front interaction stop rule will lead to errors at the edges. In the example shown the stop rule 'overlap of 5R fronts', causes a failure to stop for all fronts on the dorsal, ventral, and anterior edges (note, the wiring number of "0" along the border is due to the fact that no R-cells stopped at the correct cartridge at the end of the simulation). However, since it is unclear how the border of the lamina contributes to the stop rule, we assume that a glial, neuronal or extracellular matrix barrier prevents infinite growth cone extension. The increased error rate at the edges supports a stop rule based on R front interactions in the same way as the increased error rate at the equator: if only L-cells in the target region served as targets, neither the equator nor the edge cartridges need to exhibit errors, since edge cartridges, like equator cartridges, contain a normal complement of exactly one of each L1-L5 cells ([Meinertzhagen and Hanson, 1993](#)).

Cell

Supplemental Information

## **The Developmental Rules of Neural**

## **Superposition in *Drosophila***

Marion Langen, Egemen Agi, Dylan J. Altschuler, Lani F. Wu, Steven J. Altschuler,  
Peter Robin Hiesinger

## Supplemental Experimental Procedures

### Intravital Imaging

Pupae with the correct genotype were collected at 0 hrs after puparium formation (APF) and aged at 25°C. In preparation for imaging, the pupal case surrounding the head was removed, exposing both eyes. Double sided tape (Scotch, 3M, Cat. No. 665) was adhered to a glass slide (VWR Microscope Slides, Cat.No. 16005-106) and 0.7x0.5 cm filter paper (Fisher Scientific, Cat.No. 09-790-2F) then placed on the tape. The pupa was placed sideways on the filter paper with its right eye facing up. Another small filter paper was placed at the tip of the tail to prevent the pupa from moving. These two filter papers were moistened so that other layers of filter paper would remain in position on top of each other. Two 1.2x0.1 cm wet filter papers were placed in parallel on either side of the pupa to constitute the second layer. On top of the second layer, an additional two 1.2x0.1 cm wet filter papers were placed at the tip of the head and tail, perpendicular to the pupa's main body axis. Finally, on top of the third layer, two 1.2x0.1 cm wet filter papers were placed in parallel one on either side of the pupa as the fourth and last layer. The right eye of the pupa should be in a slightly higher position than the last layer of filter paper such that the cover slip is closest to the eye. 4% low melting point agarose (Ultra Pure Low Melting Point Agarose, Invitrogen, Cat. No. 15517-022) was applied at the points union between the wet filter paper layers to stabilize the paper tower around the pupa. Once the agarose had set, high vacuum grease (Dow Corning Corporation) was applied by a syringe around the double-sided tape to form a square wall. The thickness of the grease was slightly larger than the distance between the right eye and the glass slide. Grease served as further support for the cover slip. 1.5 µl HL3 solution (Stewart et al., 1994) was put on the cover slip (VWR micro cover glass, 22x22 mm, No.1.5, Cat.No. 48366-227) and the cover slip was placed on the pupa such that the drop of HL3 touches the pupal eye. Once the contact between the cover slip and the grease was secured and the contact between the cover slip and the pupal eye established, samples were immediately imaged. Imaging data were obtained using a Zeiss LSM 780 upright Multi-photon with a Non Descanned Detector (NDD) and an LD C-Apochromat 40x/1.1 W Korr UV-VIS-IR objective. Developing pupae were recovered from the imaging chamber after 24 hours of continuous scanning to develop in a humid chamber to adulthood. We only analyzed scanned data from pupae that subsequently developed to become healthy adults.

### Analysis of 4D data

All original 4D imaging data were processed using Amira 5.2.2 (FEI Visualization Sciences Group) using volume rendering, surface rendering and manual image segmentation tools. For each image stack at a given time point, growth cones were manually segmented and traced through all time points using the Segmentation Editor. Growth cones were identified based on morphology and cell body position. Each three-dimensional growth cone was volume rendered using a single color map. A total of 13 clusters of 2-12 growth cones were manually corrected for all rotations and aligned in a viewing angle orthogonal to the XY plane ('top view', Movies 05-17). Individual images were aligned in Adobe Photoshop. All movies were assembled in Windows Moviemaker.

To analyze the dynamics of single growth cones, coordinates were taken from heel, front, longest heel filopodium and longest growth cone front filopodium using ImageJ (NIH). These coordinates were then exported to Excel. A Matlab program was implemented to calculate the angle and length of each individual growth cone for each time point using the aforementioned coordinates. We used as measured angle the precise measurements of the longest average front filopodial angles between 30h and 35h APF. Graphs were generated in Matlab (MathWorks). Final figures were assembled in Photoshop.

To determine individual growth cone positions within the anterior-posterior axis of the lamina plexus, the lamina plexus for the last time point of each data set was manually segmented. For each data set, the last time point of individually isolated, color-coded growth cones was visualized together with the isolated lamina as a background. For each growth cone, the distance from the most anterior point to the heel and the distance between the most anterior and most posterior points were measured by SplineProbe tool of Amira 5.2.2. The ratio of the measured distances was calculated to determine the position of the growth cone along the anterior-posterior axis.

For the tracing of individual R cell axons in fixed preparations (Suppl. Fig. 1B), axons were traced as dark interiors surrounded by high-quality 24B10 stainings in conventional confocal image stacks of fixed preparations. In total, we measured 58 growth cones, including 9xR1, 6xR2, 16xR3, 12xR4, 6xR5, 9xR6 cells (Fig4B-F).

### **Implementation of the computational framework**

The three rules of growth cone sorting were implemented (in Matlab v.2014a) as follows. Refer to Supplementary Figure 3 for the following description.

The scaffolding rule: Guided by the experimental data, we constructed the "heel" grid as follows.

(1.) To create a diamond-shaped grid, we placed bundle centers (gray diamonds) down on integer lattice points and then shifted every other row in the x direction by one half.

(2.) For the dorsal portion of the grid, we placed the R1-R6 heels at equal angles apart in an ellipse around each center:  $(a \cos(\phi_n), b \sin(\phi_n))$ , with  $\phi_n = -[\alpha + (n-1)(\pi-2\alpha)/5]$  and  $n = 1$  to 6. We set  $b = 1/2$ , and solved numerically for  $a$  (the width of the ellipse) and  $\alpha$  (the offset angle from 0 or  $-\pi$  for R1 and R6 respectively), using the following two experimentally observed constraints (see Suppl. Fig. 3): (i) heels R1 and  $T_R(R5)$  have the same x position; and (ii) the differences in y positions of  $T_R(R5) - T_R(R4)$  and  $R1 - T_R(R4)$  are equal. Here,  $T_R$  is the translation of a heel by  $(1/2, 1/2)$  (see arrow in Suppl. Fig. 3). The heel positions were inverted with mirror-symmetry along the x-axis to create the ventral portion of the grid.

(3.) We warped the grid by  $10^\circ$ , as observed in the experimental data (see olive-colored diamond in figure). The grid was normalized so that the distance from a bundle center C to  $T_R(C)$  was normalized to unity (edges of diamond are length 1).

The extension and stop rules: The “idealized” direction and speed of each R-cell was computed so that all R-cells would reach the intended target at 40 hrs APF. (For simulations testing wiring robustness, the direction in which R-cells of each given type moved was altered by a randomly selected angle within the stated ranges.) Each R-cell front was assigned one of two states: “moving” or “stopped”. These states were computed based on the numbers and types of neighbors whose centers were within a prescribed sensing radius (SR). The time at which sensing began could be delayed and was set to  $1/5$  of the extension distance (corresponding to 3h after start [28h APF] unless otherwise noted. As described in the main text, this allowed us to explore combinatorial rules for stopping. When in a “moving” state, an R-cell extended linearly.

We note that in some cases “stopped” states can switch back to “moving states” due to non-transitivity of stopping conditions. For example, consider the case of a rule that tells an extending R-cell to stop if two other R-cells are nearby. Then two R-cells passing to the left and right of a third R-cell (but not near any other cells) would stop the one in the middle, but not be stopped themselves; after moving away, the middle cell could switch back to moving. This non-transitivity makes it difficult to predict theoretically the final configurations of the R-cells, and is the reason why simulations were required for this study.

Measurements of wiring accuracy: Final wiring accuracy was computed at the end of the simulation by counting the number of cells that were stopped within a Voronoi cell around each center. (A Voronoi cell around a target is the set of points that are closer to that target than any other target.) The number was compared with idealized numbers at or away from the equator.

Area overlap: For each time step during the simulation, all areas of overlap between queried R-cell (with or without target cell) were summed and then normalized by the area of the queried R-cell's sensing disk. In Fig 5G-K, only overlap with the target cell was computed; in Fig 6I overlap with all other cells was computed.

### **Supplemental References**

Meinertzhagen, I.A., and Hanson, T. (1993). The development of the optic lobe. In *The Development of Drosophila melanogaster*, M. Bate, ed. (Cold Spring Harbor: Cold Spring Harbor Laboratory Press), pp. 1363-1491.

Stewart, B.A., Atwood, H.L., Renger, J.J., Wang, J., and Wu, C.F. (1994). Improved stability of *Drosophila* larval neuromuscular preparations in haemolymph-like physiological solutions. *J Comp Physiol A* 175, 179-191.

Wolff, T., and Ready, D.F. (1991). The beginning of pattern formation in the *Drosophila* compound eye: the morphogenetic furrow and the second mitotic wave. *Development* 113, 841-850.